Supporting Information

Iron Vacancy Accelerates Biogas Slurry-Derived Fe_3O_4/Mesoporous Carbon for Water Purification

Liangmei Rao[1], Jinfeng Chen[1], Mei-rong Huang[1*], Hongguang Zhu[4,5*], Fei Yu[6], Jie Ma[1,2,3*]

[1]Research Center for Environmental Functional Materials, State Key Laboratory of Pollution Control and Resource Reuse, College of Environmental Science and Engineering, Tongji University, Shanghai, 200092, P. R. China

[2]Water Resources and Water Environment Engineering Technology Center, Xinjiang Key Laboratory of Engineering Materials and Structural Safety, School of Civil Engineering, Kashi University, Kashi 844000, PR China

[3]College of Mechanical and Energy Engineering, Tongji University, Shanghai 201804, China

[4]Shanghai Institute of Pollution Control and Ecological Security, Shanghai 200092, P.R. China

[5]Modern Agricultural Science & Engineering, Institute of Biomass Energy Research Centre, Tongji University, Shanghai 201804, P.R. China

[6]College of Oceanography and Ecological Science, Shanghai Ocean University, No 999, Huchenghuan Road, Shanghai, 201306, P. R. China

*Corresponding author

E-mail: jma@tongji.edu.cn.

1. Experimental and Discussion

1.1 Fabrication and analysis of electrode materials

Due to the exceptionally high carbon content and fluid nature of the biogas slurry, direct use without pH adjustment does not allow full exploitation of its carbon source. In this work, $Fe(NO_3)_3 \cdot 9H_2O$ was added as an iron precursor to the biogas slurry to promote thorough complexation. To assess the necessity of a hydrothermal step, a portion of the precursor–slurry mixture was adjusted to pH 10–11 with aqueous ammonia and stirred at 200 rpm for 12 h to ensure complete precipitation of $Fe(OH)_3$. The precipitate was then collected by vacuum filtration and dried, and the subsequent treatment followed exactly the same procedure used for the Fe_3O_4–C composites, yielding a non-hydrothermally processed Fe_3O_4–C sample. As shown in Fig. S1 and S2, XRD patterns of the non-hydrothermal material exhibit pronounced agglomeration and additional, unidentified diffraction peaks—indicative of residual complex ions not removed in the absence of hydrothermal treatment—while SEM images confirm extensive particle clustering.

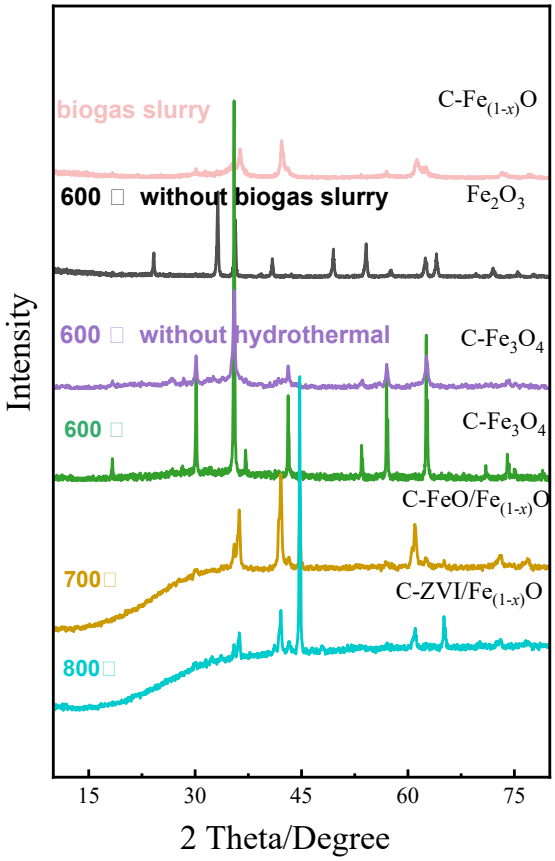

Figure S1 XRD prepared samples.

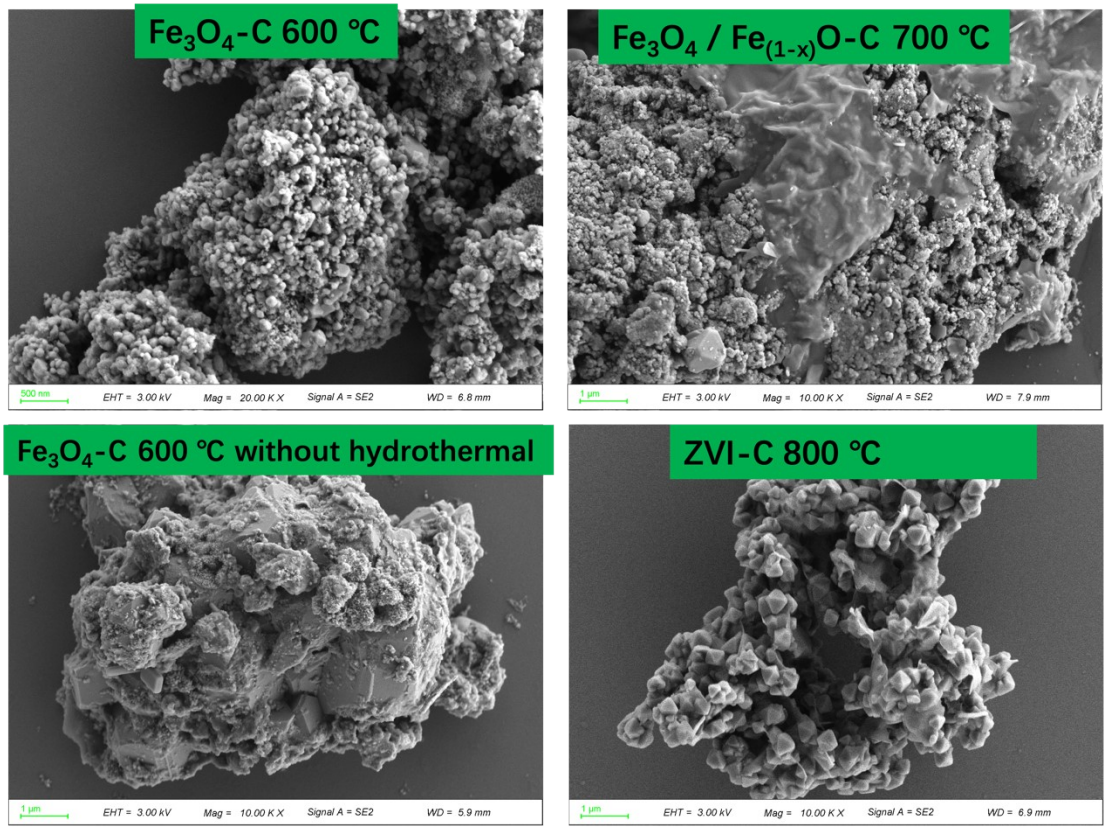

Figure S2 SEM morphology of prepared samples.

In addition, the effect of calcination temperature was evaluated at 600, 700, and 800 °C. As expected, in the absence of an external carbon source, calcination at 600 °C yielded predominantly trivalent iron oxide (Fe_2O_3). With increasing temperature and the intrinsic carbon acting as a reductant, both divalent and trivalent iron species nearly vanished at 800 °C. The SEM images in Fig. S2 reveal that the Fe^0–C (ZVI-C) sample obtained at 800 °C exhibits a markedly different morphology, and the XRD patterns in Fig. S1 display a pronounced characteristic peak at 45°, indicative of metallic iron. Therefore, under conditions of sufficient carbon availability, 600 °C was selected as the optimal calcination temperature.

Table S1 Energy Consumption of Different Desalination Technologies

Technology	Typical SEC ($kWh \cdot m^{-3}$)	Conditions/Notes	References
Membrane CDI (MCDI)	≤1.0 (target range)	Ion-exchange membranes reduce co-ion effects, enhancing charge efficiency	[1]
Reverse Osmosis, Seawater (SWRO)	3–4	State-of-the-art SWRO with energy recovery devices	[2]
Membrane Distillation (MD)	Electrical: 0.6–1.8; Thermal: significantly higher, site-dependent	Thermal energy demand is substantial; can be offset with waste heat/solar energy	[3]

Table S2 Data analysis of biogas slurry

Ca / ($mg \cdot L^{-1}$)	K / ($mg \cdot L^{-1}$)	Mg / ($mg \cdot L^{-1}$)	Na / ($mg \cdot L^{-1}$)	Cu / ($mg \cdot L^{-1}$)	Fe / ($mg \cdot L^{-1}$)	Zn / ($mg \cdot L^{-1}$)	Cd / ($mg \cdot L^{-1}$)	Cr/ ($mg \cdot L^{-1}$)
317.933	766.490	285.213	589.59	327.393	238.204	213.857	267.716	267.716
	NH_3-N / ($mg \cdot L^{-1}$)	COD / ($mg \cdot L^{-1}$)	TN / ($mg \cdot L^{-1}$)	TP / ($mg \cdot L^{-1}$)	pH	Conductivity /$ms \cdot cm^{-1}$		
	2000	3500-4000	2100	60	8.1~8.3	25		

Table S3 BET Data for Fe_3O_4-C and VFO-C

	Surface area m^2/g	Pore volume cm^3/g	micropore volume	mesopore volume
VFO-C	91.5609	0.129534	0.017768	0.111766
Fe_3O_4-C	76.4582	0.148161	0.015140	0.133021

1.2 DFT analysis

We used the DFT as implemented in the Vienna Ab initio simulation package (VASP) in all calculations. The exchange-correlation potential is described by using the generalized gradient approximation of Perdew-Burke-Ernzerhof (GGA-PBE). The projector augmented-wave (PAW) method is employed to treat interactions between ion cores and valence electrons. The plane-wave cutoff energy was fixed to 400 eV. Given structural models were relaxed until the Hellmann–Feynman forces smaller than -0.02 eV/Å and the change in energy smaller than 10^{-5} eV was attained. The vacuum thickness was set to be 25 Å to minimize interlayer interactions. During the relaxation, the Brillouin zone was represented by a Γ centered k-point grid of 1×1×1. Grimme's DFT-D3 methodology was used to describe the dispersion interactions among all the atoms in adsorption models.

1.3 Process and analysis of desalination

1.3.1 Salt Adsorption Capacity

The salt adsorption capacity (SAC, $mg \cdot g^{-1}$) quantifies the mass of salt removed per unit mass of electrode material. It is calculated from the change in solution concentration before and after electrosorption as follows:

$$SAC = \frac{(C_0 - C_e) \times V}{m}$$

Where C_o: initial salt concentration ($mg\ L^{-1}$);

C_e: equilibrium salt concentration ($mg\ L^{-1}$);

V: solution volume (L);

m: mass of electrode material (g).

1.3.2 Average Salt Adsorption Rate

The average salt adsorption rate (ASAR, mg·g^{-1}·s^{-1}) reflects the speed of ion removal and is defined as:

$$ASAR = \frac{SAC}{t}$$

SAC: salt adsorption capacity (mg g^{-1});

t: adsorption time (s).

1.3.3 Charge Efficiency

Charge efficiency (Λ) evaluates the fraction of electric charge that contributes to ion removal. Under ideal conditions all electrode charge is used for ion adsorption ($\Lambda = 1$), but in practice co-ion effects and ion rearrangement reduce Λ. It is calculated by:

$$\Lambda = \frac{\Gamma \times F}{\Sigma}$$

Where Γ: molar adsorption capacity (mol g^{-1}), given by

$$\Gamma = \frac{SAC}{58.5 \times 1000}$$

F: Faraday constant (96 485 C mol^{-1});

Σ: total charge consumed during adsorption (C g^{-1}), given by

$$\Sigma = \frac{\int i \mathrm{d}t}{m}$$

with i = current (A), t = time (s), and m = electrode mass (g).

1.3.4 Energy Consumption

Energy-normalized adsorbed salt (ENAS, mg·J^{-1}) is widely used to assess the practical viability of an electrode material by quantifying the mass of salt removed per unit of energy consumed. In a constant-voltage electrosorption test, ENAS is defined as:

$$ENAS = \frac{SAC \times m}{U \times \int i dt}$$

where

SAC: salt adsorption capacity (mg·g^{-1});

m: mass of electrode material (g);

U: applied voltage (V);

i : charging current (A).

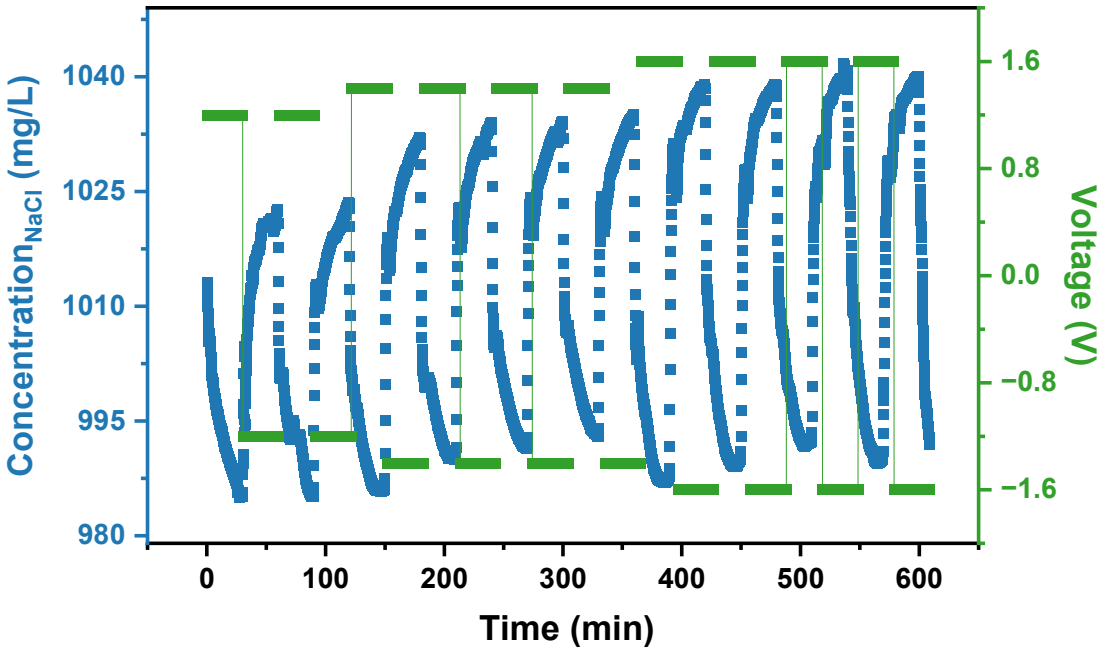

Figure S3 Concentrations responses of Fe_3O_4-C electrode versus various cut-off voltage.

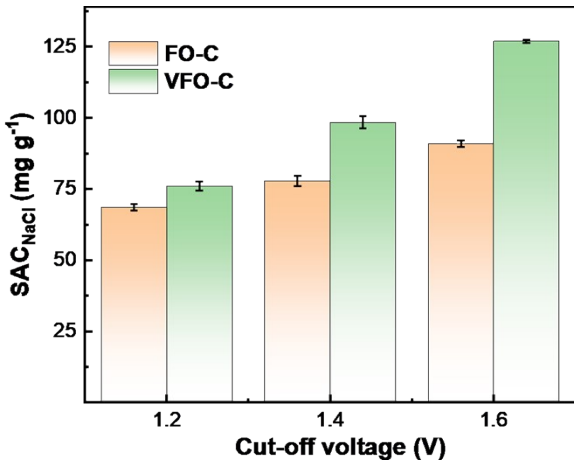

Figure S4 SACs of VFO-C electrode and Fe_3O_4-C electrode at different cut-off voltages.

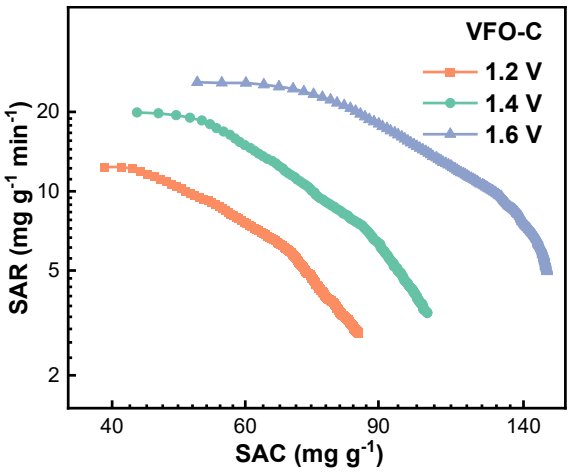

Figure S5 Ragone plots of VFO-C at different cut-off voltages.

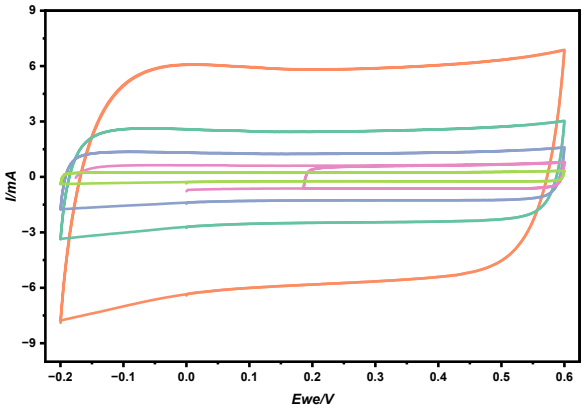

Figure S6 CV curves of biogas slurry based carbon at 1-50 mV s^{-1}

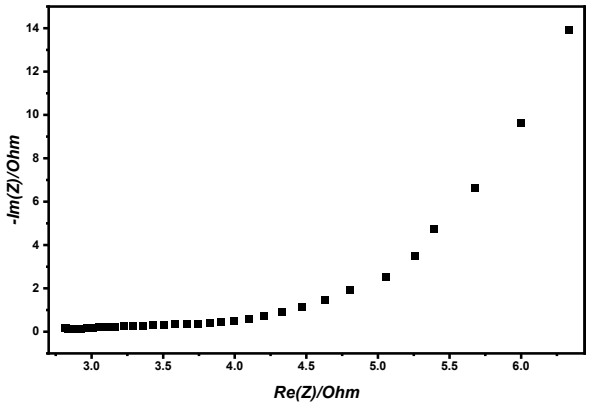

Figure S6 Nyquist plots of biogas slurry based carbon

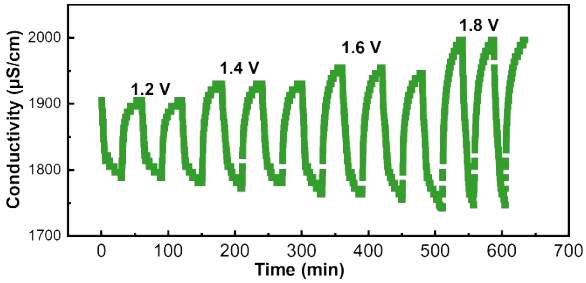

Figure S7 Conductivity responses (1000 mg L^{-1} NaCl) of carbon baesd electrode versus various cut-off voltage.

References

(1) Porada, S.; Zhang, L.; Dykstra, J. E. Energy consumption in membrane capacitive deionization and comparison with reverse osmosis. *Desalination* **2020**, *488*, 114383.

(2) Kim, J.; Park, K.; Yang, D. R.; Hong, S. A comprehensive review of energy consumption of seawater reverse osmosis desalination plants. *Appl. Energy* **2019**, *254*, 113652.

(3) López-Porfiri, P.; Ramos-Paredes, S.; Núñez, P.; Gorgojo, P. Towards the technological maturity of membrane distillation: the MD module performance curve. *NPJ Clean Water* **2023**, *6*, 18-19.